Nano Research
DOI 10.1007/s12274-014-0551-7
Research Article
ISSN 1998-0124
CN 11-5974/O4

Field-effect passivation on silicon nanowire solar cells

Anna Dalmau Mallorquí[1], Esther Alarcón-Lladó[1], Ignasi Canales Mundet[1], Amirreza Kiani[1], Bénédicte Demaurex[2], Stefaan De Wolf[2], Andreas Menzel[3], Margrit Zacharias[3], and Anna Fontcuberta i Morral[1] (✉)

[1] *Laboratoire des Matériaux Semiconducteurs, École Polytechnique Fédérale de Lausanne, 1015 Lausanne, Switzerland*
[2] *Photovoltaics and Thin Film Electronics Laboratory, Institute of Microengineering (IMT), École Polytechnique Fédérale de Lausanne, 2000 Neuchâtel, Switzerland*
[3] *Nanotechnology, Institute of Microsystems Engineering (IMTEK), Albert-Ludwigs-University, 79110 Freiburg, Germany*

Received: 25 May 2014
Revised: 7 July 2014
Accepted: 31 July 2014

KEYWORDS
field-effect,
passivation,
nanowire,
surface recombination,
solar cell

ABSTRACT

Surface recombination represents a handicap for high-efficiency solar cells. This is especially important for nanowire array solar cells, where the surface-to-volume ratio is greatly enhanced. Here, the effect of different passivation materials on the effective recombination and on the device performance is experimentally analyzed. Our solar cells are large area top-down axial n–p junction silicon nanowires fabricated by means of Near-Field Phase-Shift Lithography (NF-PSL). We report an efficiency of 9.9% for the best cell, passivated with a SiO_2/SiN_x stack. The impact of the presence of a surface fixed charge density at the silicon/oxide interface is studied.

1 Introduction

Semiconductor nanowires have received increasing attention for next-generation solar cells technology [1–8]. One of the most important challenges these devices face is surface recombination. Surface recombination is a major concern for nanowire array solar cells due to their high surface-to-volume ratio. Their photovoltaic performance is seriously reduced by the presence of surface dangling bonds, which act as recombination centers [9]. It has been experimentally demonstrated that by reducing the surface recombination by almost two orders of magnitude the light absorption cross-section of the wire increases for a broad range of wavelengths and its photosensitivity enhances 90-fold when used as a photodetector [10]. It has also been shown that minority carrier lifetime is controlled by the surface recombination and strongly depends on the nanowire diameter [11, 12].

The reduction in the surface recombination (SR) rate of nanowire-based solar cells results in an increase of open-circuit voltage, short-circuit current and efficiency [5, 13, 14]. However, the effect of the SR rate strongly depends on the junction configuration.

Address correspondence to anna.fontcuberta-morral@epfl.ch

Yu et al. simulated the impact of surface recombination velocity on both axial and radial p–n junction nanowire arrays [15], and they concluded that the recombination rate at the surface for the same doping level is higher in the axial configuration than in the radial one.

Among the many different materials investigated for passivation purposes, thermal SiO_2 [16–18], a-SiN_x:H [19–21], Al_2O_3 [22–24] or the SiO_2/SiN_x bilayer [25] are some of the most widely used. We have studied experimentally the effect of these materials on the surface passivation of axial n–p junction Si nanowires. To this end, ordered arrays of nanowires were fabricated by Near-Field Phase-Shift Lithography (NF-PSL), a photolithographic-based technique that allows to obtain large areas of submicron structures by manipulating the incident light [26]. The interface between the silicon and the passivation material and their passivation properties were analyzed as well as their influence on the photoconversion efficiency.

2 Experimental

Axial n–p junction nanowires were fabricated by means of a two-step near-field phase-shift lithography as reported elsewhere [27]. Below we give the details of the fabrication process of the mask and nanowire array solar cells, including the passivation step.

2.1 Mask fabrication

A key issue to increase the resolution of NF-PSL is to fabricate a grating mask with very sharp phase edges. This leads to a higher and narrower peak of the intensity profile of interference waves on the resist layer. For this reason, electron beam lithography was used to write the design on the phase-shift mask, as it provides higher resolution than other techniques. Additionally, fused silica was the material chosen for the mask. Its high purity results in vertical and sharp sidewalls after etching.

In order to avoid electrostatic charging during electron beam lithography, a layer of 100 and 350 nm of aluminum was sputtered on the front and back side of the mask, respectively. 150 nm of ZEP520A resist (consisting of 11% methyl styrene and chloromethyl acrylate copolymer and 89% anisole), diluted 50% in anisole was spin-coated before performing electron beam lithography. Following the work of Wang et al. [28], arrays of 4 mm × 4 mm were patterned with 2-μm wide trenches spaced 4 μm apart. After development, resist-free aluminum regions were exposed for 20 s to induced coupled plasma etching using a Cl_2/BCl_3 gas mixture (STS Multiplex ICP). Afterwards, a long O_2 plasma strip was performed to completely remove all the ZEP resist. Subsequently, using the aluminum layer as hard mask, the pattern was transferred to the fused silica substrate by means of a C_4F_8/CH_4 plasma etching for 130 s, leading to a groove depth of 500 nm. Finally, aluminum was stripped off by an aluminum etchant ANP (H_3PO_4 (85%) + CH_3COOH (100%) + HNO_3 (70%) + H_2O, 83:5:5:5) dip for around 30 min.

2.2 Nanowire array solar cells

380-μm thick Czochralski<100>p-doped Si wafers with a resistivity of 1–10 Ω·cm (corresponding to a doping concentration of ~10^{15} cm^{-3} were used). Prior to the fabrication of the nanowires, the n-emitter was formed by diffusing $POCl_3$ for 15 min at a temperature of 950 °C. Under these conditions the junction depth, determined by capacitance–voltage measurements (Wafer Profiler CVP21), was 1.2 μm. In order to ensure that only the front side was doped, the back of the wafer had been coated with a 200-nm thick SiO_2 diffusion barrier layer. Immediately after the diffusion process, the back-side oxide was stripped-off with buffered HF.

Axial n–p junction nanowires were created etching down nanoscale dots on the n–p silicon substrate. The steps carried out to fabricate the Si nanowire arrays are depicted in Fig. 1. A first standard photolithography step was carried out to create the alignment marks, required to correctly align the substrate and the mask between the first and the second NFC-PSL steps. For this, the Si wafer was coated by 1.1 μm of AZ1512H photoresist and exposed for 1.6 s. Silicon was etched for 2 min in wet etchant (HNO_3 (70%) + HF (49%) + H_2O, 5:3:20). The photoresist was removed by exposing the wafer under plasma O_2.

After coating the wafer with 650 nm of AZ ECI 3007 positive photoresist, it was exposed for 1.4 s under UV broad band light (Hg light source UV400: g, h, i-line) with a power intensity of 10 mW/cm^2 (Fig. 1(a)). This step was repeated after rotating the mask 90° (Fig. 1(b)).

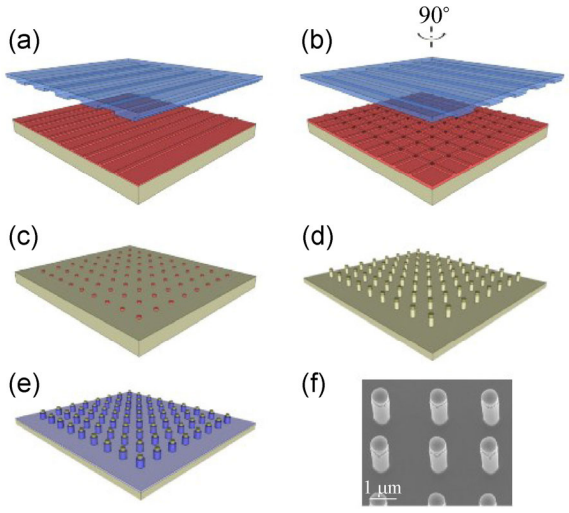

Figure 1 Schematic of the fabrication of axial n–p junction nanowires by PSL: (a) and (b) Double-step NF-PSL; (c) array of 600-nm dots after NF-PSL; (d) array of nanowires after reactive ion etching; and (e) array of nanowires coated with partially etched oxide. (f) SEM image tilted 25° of PSL-fabricated nanowires.

The first exposure led to an array of stripes aligned following the *x*-axis, while the second one defined the identical array of stripes in the perpendicular direction, creating overexposed nanoscale dots at the intersection. The two exposures were done consecutively and afterwards the photoresist was developed following standard photolithography procedures (Fig. 1(c)). For this double-step lithography, a vacuum contact between the mask and the wafer was required. We obtained arrays of nanowires with a diameter of 600 nm (Fig. 1(f)).

The PSL pattern was transferred to the silicon substrate by means of reactive ion etching (SF_6 (40 sccm)/C_4F_8 (55 sccm) gas mixture) for 4 min and, subsequently, the remaining photoresist was removed. This etching time led to a pillar height of around 2 μm.

After fabricating the nanowires, a dielectric barrier was deposited conformally all over the front surface. This layer has a double function: To electrically insulate the n and p regions and to passivate the surface. The performance of four different materials was compared: (i) Al_2O_3 deposited by atomic layer deposition (ALD, Beneq TFS200) using trimethylaluminum (TMA) as the precursor and H_2O as the oxidant at 200 ˚C; (ii) SiO_2 thermally grown at 1,000 ˚C in oxygen gas for 47 min followed by a nitrogen anneal at the same temperature; (iii) a-SiN_x:H deposited by plasma enhanced chemical vapour deposition (PECVD) (Oxford PlasmaLab 100 PECVD) at a temperature of 300 ˚C, a pressure of 800 mTorr and a gas mixture of 2% SiH_4/N_2 = 1,000 sccm and NH_3 = 15 sccm; and (iv) a bilayer of thermally-grown-SiO_2/PECVD-SiN_x. We estimate that after the growth of the thermal oxide layer the junction is shifted around 100 nm.

In order to selectively contact the n-type region, the insulating barrier was partially etched at the nanowire tip. For this, a 3,100-nm thick film of photoresist was spin-coated at 3,000 rpm for 1 min and post-baked at 120 ˚C for 5 min. Afterwards, the polymer layer was etched down to a final thickness of 1,800 ± 100 nm by means of an O_2 Induced Coupled Plasma etching (ICP). A controlled etch was achieved by using an electrostatic chuck power of 100 W and an ICP source power of 600 W. The controllability of the polymer etching is extremely important to avoid short-circuit between the front contact and the p-doped base. In our case, the junction depth is around 1.2 μm and the nanowires are about 2 μm long. After etching, the polymer exhibited a thickness of 1.3 μm. All dielectrics were etched by dipping the sample in buffered HF (BHF 7:1, NH_4F (40%) + HF (50%)) solution for 20 or 50 s, depending on the thickness and nature of the layer (Fig. 1(e)). A last O_2 plasma removal was carried out to clean the sample from any polymer residue. Finally, the front and backside contacts were deposited by sputtering: 500 nm of indium tin oxide (ITO) on the front side and 200 nm of aluminum on the backside. On top of the ITO, a "ring" of 10 nm of Ti and 100 nm of Au was evaporated through a metallic mask around the array. A cross-section of the final device is depicted in Fig. 2. 12 devices of 16 mm^2 were prepared for each type of passivation.

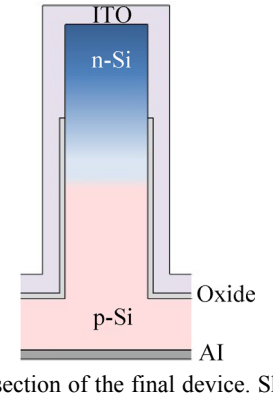

Figure 2 Cross-section of the final device. Sketch not drawn to scale.

3 Results

The current–voltage characteristics of NF-PSL nanowire-based solar cells passivated with the four different dielectrics were measured in the dark and under illumination conditions of AM 1.5G (Sol2A Oriel 150 W Xenon lamp) and are shown in Fig. S1 (in the Electronic Supplementary Material (ESM)), Fig. 3 and Table 1. As expected, surface recombination on axial p–n junction nanowire arrays have a significant impact on the short-circuit current density (J_{sc}) and open-circuit voltage (V_{oc}). Comparing the four curves, it can be observed that the devices passivated with SiN_x and Al_2O_3 have similar V_{oc} and J_{sc}, yielding to efficiencies (η) of 3.4% and 2.4%, respectively. On the other hand, it is well-known that thermally grown SiO_2 leads to a high quality interface and reduced surface recombination. Unexpectedly, the device passivated with thermal SiO_2 reports the worst results (J_{sc} = 11.3 mA/cm^2, V_{oc} = 0.22 V and η = 1.2%). Interestingly, the addition of the outermost 19-nm-thick SiN_x layer greatly enhances the photovoltaic properties of the device: $J_0 = 1.1 \times 10^{-4}$ mA/cm^2, J_{sc} = 28.4 mA/cm^2, V_{oc} = 0.52 V, FF = 0.67 and η = 9.9%.

In order to understand the performance differences of the various passivating materials, the minority carrier lifetime was measured by means of quasi-steady-state photoconductance (QssPC) measurements (WCT-100 Sinton Instruments) [29]. For these measurements, we recreated the device interfaces on the two sides of a non-textured Si wafer. We first etched down both surfaces with reactive ion etching in order to have the same surface roughness as on the nanowire sidewalls and then deposited the passivation layer. The effective lifetimes, τ_{eff}, were extracted at an injection level of 10^{15} cm^{-3} and are summarized in Table 1. The diffusion length, L, and surface recombination velocity, S_{eff}, are calculated from τ_{eff} by the following expressions

$$L = \sqrt{\tau_{eff} D}$$

and

$$\frac{1}{\tau_{eff}} = \frac{1}{\tau_{bulk}} + \frac{2S_{eff}}{W}$$

where D is the carrier diffusivity (D = 34.41 cm^2/s for a doping level of $N_A = 10^{15}$ cm^{-3}) [30] and W is the wafer thickness (W = 380 μm). Considering that $\tau_{bulk} \gg \tau_{surf}$,

$$\frac{1}{\tau_{eff}} \approx \frac{2S_{eff}}{W}$$

Based on QssPC results, thermal SiO_2 presents the best level of surface passivation, as it leads to the highest lifetime (τ_{eff} = 46 μs), followed by the SiO_2/SiN_x bilayer, SiN_x and Al_2O_3. Nonetheless, the low surface recombination values do not result in a better solar cell performance.

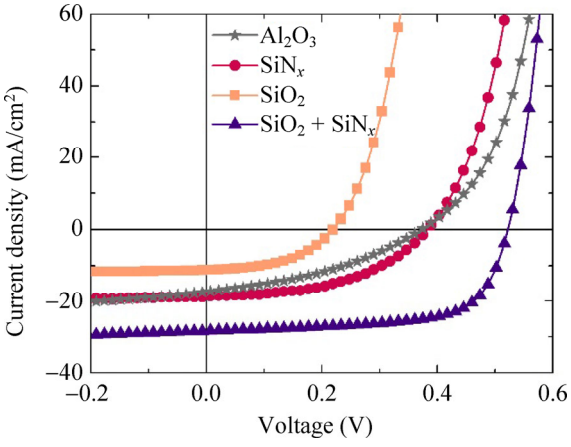

Figure 3 Current–voltage characteristics under AM 1.5G illumination of the nanowire arrays covered with Al_2O_3, SiN_x, SiO_2 and a SiO_2/SiN_x bilayer.

Table 1 Solar cell characteristics and passivation qualities with respect to the passivation layer

Passivating material	Film thickness (nm)	τ_{eff} (μs)	S_{eff} (cm/s)	L_{eff} (μm)	J_0 (mA/cm^2)	J_{sc} (mA/cm^2)	V_{oc} (V)	FF	η (%)
Al_2O_3	44	13	1462	212	0.073	17.4	0.37	0.38	2.4
SiN_x	52	19	1000	257	0.065	18.7	0.38	0.48	3.4
SiO_2	48	46	413	398	0.89	11.3	0.22	0.48	1.2
SiO_2/SiN_x	52/19	38	500	362	1.1×10^{-4}	28.4	0.52	0.67	9.9

In order to shed some more light in the difference between SiN_x, SiO_2 and SiO_2/SiN_x passivation in the solar cell performance, an analysis of the chemical composition of the interface between the Si substrate and the passivation layer was carried out by Fourier transform infrared (FTIR) spectroscopy using the attenuated total reflection (ATR) mode (6700 Nicolet, Thermo Fisher Scientific). From FTIR measurements, information about the different bonding configurations at the interface are obtained, which can be related to chemical and field-effect passivation. In Fig. 4 the FTIR spectra of Si–SiO_2, Si–SiN_x and the bilayer Si–SiO_2/SiN_x are compared.

The spectrum of the SiN_x film presents several peaks around 840, 2,160 and 3,350 cm^{-1} corresponding respectively to the Si–N, Si–H and N–H bonds [31]. The Si–H stretching bond can be deconvoluted into six Gaussian peaks: H–Si–Si_3 around 2,000 cm^{-1}, H–Si–HSi_2 around 2,060 cm^{-1}, H–Si–NSi_2 around 2,100 cm^{-1}, H–Si–SiN_2 and H–Si–SiNH around 2,140 cm^{-1}, H–Si–HN_2 around 2,170 cm^{-1} and H–Si–N_3 around 2,220 cm^{-1}. Mäckel and Lüdemann related the presence of N–H bonds to the formation of the ·Si≡Si_3 dangling bond, the so-called K^+ center. This leads to a fixed positive charge density, Q_f, of the order of 10^{12} cm^{-2} [32].

The spectrum of thermally grown SiO_2 exhibits the characteristic peaks at 810, 1,060 and 1,250 cm^{-1} corresponding respectively to the vibrational bending, and transversal optical (TO) and longitudinal optical (LO) modes of the stretching bands of Si–O–Si [18]. Thermal SiO_2 provides a high level of chemical passivation on Si surfaces due to its low interface defect density ~10^{10} cm^{-2}. The trivalently bonded Si atom with one dangling bond (·Si≡Si_3), known as P_b center, is the main defect at Si/SiO_2 interfaces due to a lattice mismatch. These defects lead to positive Q_f of the order of 10^{10} cm^{-2} [33]. They are generally passivated by a hydrogen post-treatment. For instance, the addition of a hydrogen-containing capping layer results in a hydrogen passivation of the interface. In good agreement with this, we observe the appearance of the Si–H signal at 2,160 cm^{-1} of the SiO_2/SiN_x spectrum in comparison to the single SiO_2 layer. One should also note that the addition of the SiO_2 interlayer between Si and SiN_x reduces significantly the concentration of Si–N bonds in comparison with the Si/SiN_x interface. Both, the H-passivation of the interface and the reduction of the Si–N bonds, result in a no field-effect passivation by the SiO_2/SiN_x stack [34].

We comment now on the Al_2O_3 passivation. The FTIR spectrum of the Al_2O_3 film shown in Fig. 5 exhibits the characteristic Al–O absorption peak at 704 cm^{-1}. The presence of a thin SiO_x interlayer formed during the ALD deposition process is elucidated by the existence of a broad peak at 940–1,100 cm^{-1} [35]. Hoex et al. suggested that this interfacial layer could induce a high density of Al vacancies at the interface [24]. Some theoretical studies have concluded that Al vacancies and O interstitial can be charged negatively [36], leading to negative Q_f values in the range of 10^{12}–10^{13} cm^{-2}.

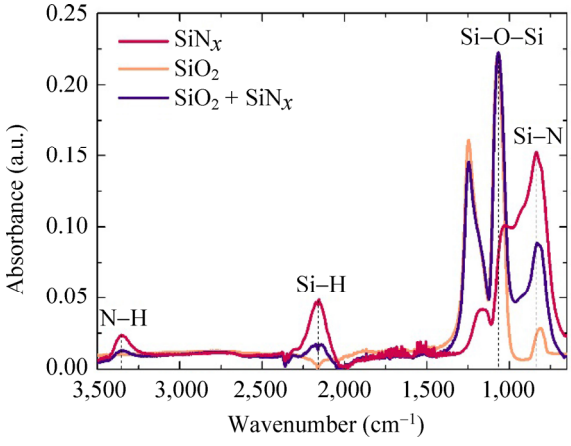

Figure 4 FTIR spectra of the Si/SiN_x, Si/SiO_2 and Si/SiO_2 + SiN_x interfaces.

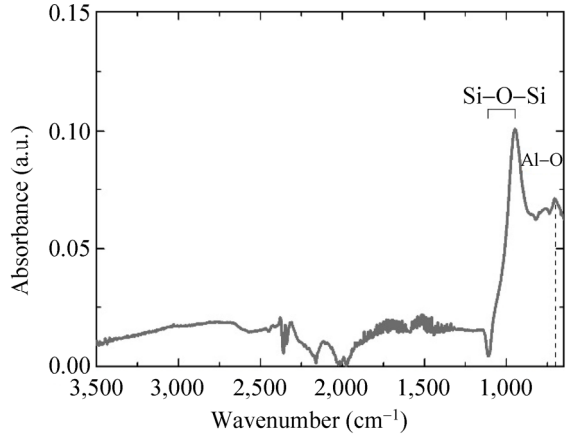

Figure 5 FTIR spectrum of the Si/Al_2O_3 interface.

The effect of the presence of fixed charges at the silicon/insulator interface of the nanowire sidewall in terms of band bending [37, 38] was investigated with the simulation software next**nano**^{3} [39]. In Fig. 6 we show the results of the calculations. The electron and hole density profiles in the cross-section of 600 nm wide nanowires is shown for a positive fixed charge of $Q_f = 3 \times 10^{10}$, 10^{11} and 10^{12} cm^{-2}. For the calculations we used a doping concentration of $N_A = 10^{15}$ cm^{-3}. The positive charge creates an electric field that attracts electrons towards the surface and pushes holes towards the center of the nanowire. The low p-doping concentration results in inverted doping conditions for high Q_f values ($\geqslant 10^{11}$ cm^{-2}). Electrons become majority carriers while holes get reduced to minority carriers within the whole nanowire cross-section. In such a case, the junction is shifted to the base of the nanowire. For $Q_f = 3 \times 10^{10}$ cm^{-2} no inversion occurs on planar surfaces, which explains the high lifetime values measured for SiO_2-passivated devices. Nevertheless, the effect of the same density of fixed charges on a nanoscale cylinder geometry is remarkable. In this configuration, inversion conditions occur at the surface and the electron and hole densities become equal at some regions inside the nanowire cross-section, resulting in a significant increase of recombination inside the wire. As mentioned above, this could be the case of SiO_2-passivated devices, whose interfaces typically exhibit a low density of fixed positive charges. These results are in agreement with the high dark current density (J_0) exhibited by these devices and could explain their poor performance. Interestingly, the high density of fixed charges introduced by the Si/SiN_x interface results in a n-doped-like nanowire and the junction is moved to the base of the wire, resulting in a reduction of surface recombination in the nanowire ($J_0 = 1.1 \times 10^{-4}$ mA/cm^{-2}).The external quantum efficiency (EQE) results shown in Fig. S2 (in the ESM) also reflect the impact of changing the fixed charge density on the photoconversion efficiency.

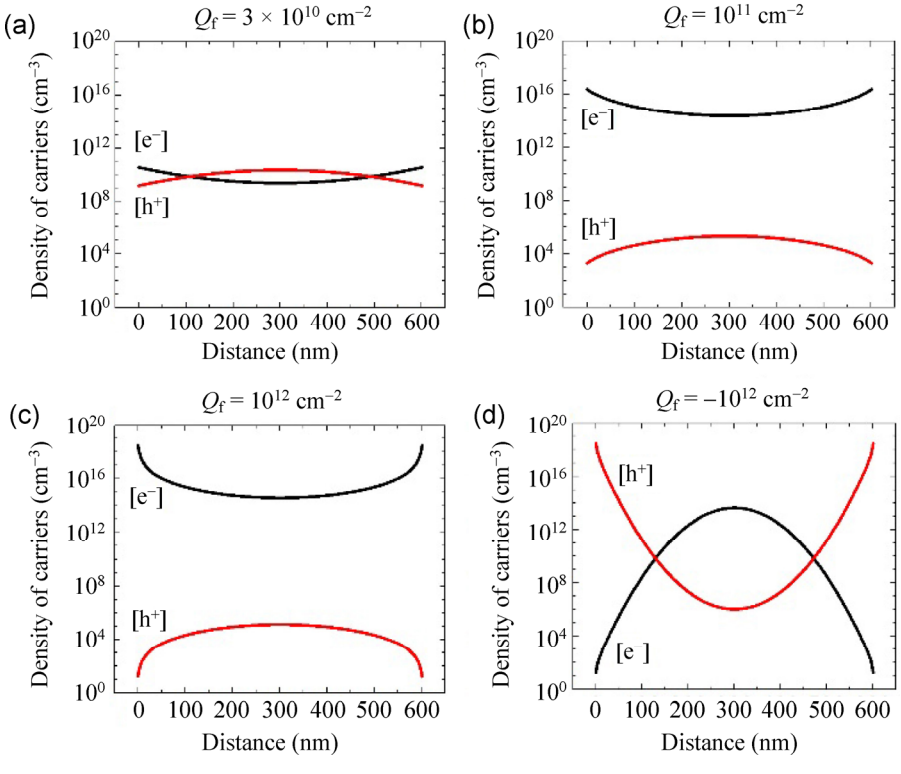

Figure 6 Carrier density profile across the p-doped Si nanowire cross-section ($N_A = 10^{15}$ cm^{-3}) under the influence of a positive fixed charge of (a) $Q_f = 3 \times 10^{10}$, (b) 10^{11} and (c) 10^{12} cm^{-2}. (d) Carrier density profile at the n-doped nanowire cross-section ($N_D = 10^{16}$ cm^{-3}) with a negative fixed charge of $Q_f = -10^{12}$ cm^{-2}. Black lines show the evolution of hole density with Q_f and red lines depict electron density.

The negative nature of the fixed charges in the Si–Al_2O_3 system results in a different outcome. At the p-region of the wire, the fixed charges create an electric field that shields electrons from the surface. However, since the Al_2O_3 layer partially covers the n-doped region of the wire, an inversion occurs at this point. Figure 6(d) shows what is the impact of a -10^{12} cm^{-2} fixed charge on a n-doped region with a doping concentration of $N_D = 10^{16}$ cm^{-3}. Also here, there is an inversion of electron and hole densities at some regions of the nanowire exhibiting an equivalent concentration of electrons and holes, resulting in an enhancement of the recombination. In order to illustrate the results of the calculations more explicitly, we sketch in a qualitative manner the distribution of carriers in the nanowires for the four types of passivation (Fig. 7).

Finally, the light absorption in the device was calculated by Finite Difference Time-Domain (FDTD) simulations reaching steady-state conditions [40]. The incoming light was modeled as a plane wave polarized along the x-direction with an incidence normal to the structure. The calculations were realized for a realistic configuration of the nanowire device: An array of 2 μm long Si nanowires with a diameter of 600 nm, a pitch of 2 μm and a passivation layer of 50 nm of silicon dioxide covering the substrate and the nanowire sidewalls up to a height of 1.5 μm and a layer of 400 nm of ITO as front electrode. Figure 8 depicts the normalized electric field energy density along the wire (at $x = 0$ and $y = 0$) and within the wire cross-section at 400 nm below the junction respectively, at 400, 600, 800 and 1,000 nm. From the vertical cross-section, it can be observed that light is mainly absorbed within the wire, even though the nanowires are fairly short and silicon exhibits an indirect band gap. As a consequence, most of the photogenerated carriers in the devices are generated in the nanowires and the substrate exhibits a minor role. From this, we conclude that the major losses must be due to carrier recombination in the wire. This is especially harmful for the SiO_2- and Al_2O_3-passivated devices but also for the one coated with SiN_x, as the junction is shifted further away from the generated carriers and more of them recombine before reaching the junction.

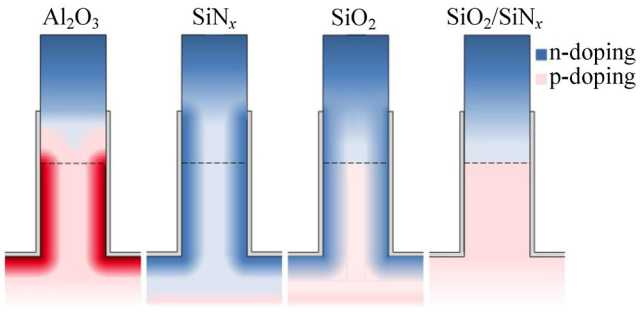

Figure 7 Qualitative illustration of the carrier density profile across the nanowire under the influence of interface fixed charges induced by the different passivation materials. Bluish and reddish areas depict n-doped and p-doped regions, respectively. Black dashed lines depict the initial position of the junction.

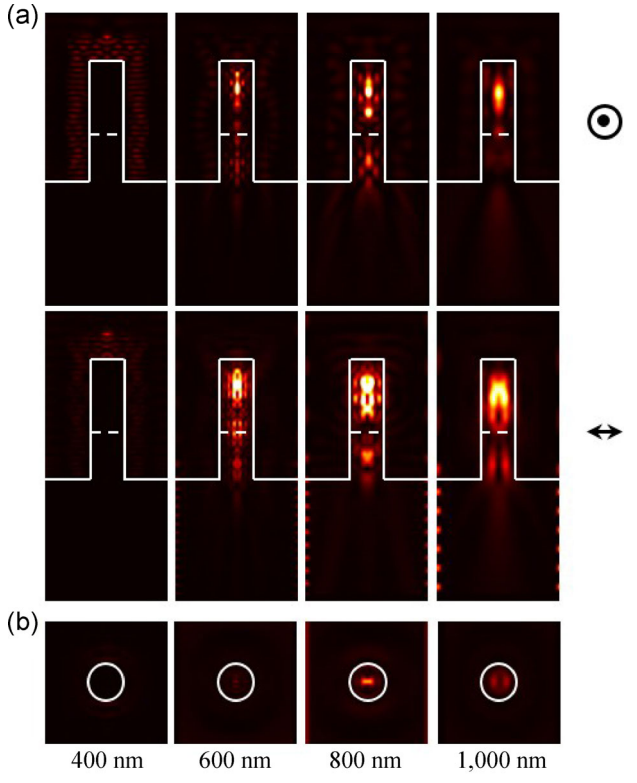

Figure 8 FDTD simulated electric field energy density (a) along the z-axis (above: Cross-section at $x = 0$; below: Cross-section at $y = 0$) and (b) at the cross-section placed 400 nm above the base of the Si nanowire (400 nm below the junction) at 400, 600, 800 and 1,000 nm.

4 Conclusions

The role of surface recombination on the performance of axial n–p junction Si nanowire-based solar cells has been investigated. Si nanowire arrays have

been fabricated by means of NF-PSL. Four different passivation materials have been analyzed: ALD Al_2O_3, thermal SiO_2, PECVD SiN_x and a SiO_2/SiN_x stack. It has been demonstrated that, even having a high level of chemical passivation at the interface, the presence of a surface fixed charge density can lead to an inversion of carrier densities or to an enhancement of the recombination rate within the nanowire core. This effect is more important on nanowires due to their small diameters. The addition of a hydrogen-containing capping layer, which leads to a hydrogen passivation of dangling bonds and to the suppression of fixed charges at the interface, can nullify this effect. The device passivated with the SiO_2/SiN_x stack reported the best results, exhibiting a J_{sc} of 28.4 mA/cm^2, a V_{oc} of 0.52 V and an efficiency of 9.9%.

Acknowledgements

Funding through ERC Stg UpCon and Nano Tera Synergy are greatly acknowledged. B. D. acknowledges financial support by European Community's FP7 Program under Hercules Project, EuroTech Universities Alliance and AxpoNaturstromFonds Switzerland.

Electronic Supplementary Material: Supplementary material (current–voltage measurements in the dark) is available in the online version of this article at http://dx.doi.org/ 10.1007/s12274-014-0551-7.

References

[1] Duan, X. F.; Huang, Y.; Cui, Y.; Wang, J. F.; Lieber, C. M. Indium phosphide nanowires as building blocks for nanoscale electronic and optoelectronic devices. *Nature* **2001**, *409*, 66–69.

[2] Kelzenberg, M. D.; Boettcher, S. W.; Petykiewicz, J. A.; Turner-Evans, D. B.; Putnam, M. C.; Warren, E. L.; Spurgeon, J. M.; Briggs, R. M.; Lewis, N. S.; Atwater, H. A. Enhanced absorption and carrier collection in Si wire arrays for photovoltaic applications. *Nat. Mater.* **2010**, *9*, 239–244.

[3] Polman, A.; Atwater, H. A. Photonic design principles for ultrahigh-efficiency photovoltaics. *Nat. Mater.* **2012**, *11*, 174–177.

[4] Czaban, J. A.; Thompson, D. A.; LaPierre, R. R. GaAs core-shell nanowires for photovoltaic applications. *Nano Lett.* **2009**, *9*, 148–154.

[5] Cui, Y. C.; Wang, J.; Plissard, S. R.; Cavalli, A.; Vu, T. T. T.; van Veldhoven, R. P. J.; Gao, L.; Trainor, M.; Verheijen, M. A.; Haverkort, J. E. M. et al. Efficiency enhancement of InP nanowire solar cells by surface cleaning. *Nano Lett.* **2013**, *13*, 4113–4117.

[6] Wallentin, J.; Anttu, N.; Asoli, D.; Huffman, M.; Aberg, I.; Magnusson, M. H.; Siefer, G.; Fuss-Kailuweit, P.; Dimroth, F.; Witzigmann, B. et al. InP nanowire array solar cells achieving 13.8% efficiency by exceeding the ray optics limit. *Science* **2013**, *339*, 1057–1060.

[7] Krogstrup, P.; Jørgensen, H. I.; Heiss, M.; Demichel, O.; Holm, J. V.; Aagesen, M.; Nygard, J.; Fontcuberta i Morral, A. Single-nanowire solar cells beyond the Shockley-Queisser limit. *Nat. Photonics* **2013**, *7*, 306–310.

[8] Yu, L. W.; Misra, S.; Wang, J. Z.; Qian, S. Y.; Foldyna, M.; Xu, J.; Shi, Y.; Johnson, E.; Roca i Cabarrocas, P. Understanding light harvesting in radial junction amorphous silicon thin film solar cells. *Sci. Rep.* **2014**, *4*, 4357.

[9] Fernández-Serra, M. V.; Adessi, C.; Blase, X. Conductance, surface traps, and passivation in doped silicon nanowires. *Nano Lett.* **2006**, *6*, 2674–2678.

[10] Dan, Y. P.; Seo, K.; Takei, K.; Meza, J. H.; Javey, A.; Crozier, K. B. Dramatic reduction of surface recombination by *in situ* surface passivation of silicon nanowires. *Nano Lett.* **2011**, *11*, 2527–2532.

[11] Demichel, O.; Heiss, M.; Bleuse, J.; Mariette, H.; Fontcuberta i Morral, A. Impact of surfaces on the optical properties of GaAs nanowires. *Appl. Phys. Lett.* **2010**, *97*, 201907.

[12] Joyce, H. J.; Wong-Leung, J.; Yong, C. K.; Docherty, C. J.; Paiman, S.; Gao, Q.; Tana, H. H.; Jagadish, C.; Lloyd-Hughes, J.; Herz, L. M. et al. Ultralow surface recombination velocity in InP nanowires probed by terahertz spectroscopy. *Nano Lett.* **2012**, *12*, 5325–5330.

[13] Holm, J. V.; Jørgensen, H. I.; Krogstrup, P.; Nygård, J.; Liu, H. Y.; Aagensen, M. Surface-passivated GaAsP single-nanowire solar cells exceeding 10% efficiency grown on silicon. *Nat. Commun.* **2013**, *4*, 1498.

[14] Kim, D. R.; Lee, C. H.; Rao, P. M.; Cho, I. S.; Zheng, X. L. Hybrid Si microwire and planar solar cells: Passivation and characterization. *Nano Lett.* **2011**, *11*, 2704–2708.

[15] Yu, S. Q.; Roemer, F.; Witzigmann, B. Analysis of surface recombination in nanowire array solar cells. *J. Photon. Energy* **2012**, *2*, 028002.

[16] Deal, B. E.; Grove, A. S. General relationship for the thermal oxidation of silicon. *J. Appl. Phys.* **1965**, *36*, 3770–3778.

[17] Zhao, J. H.; Wang, A. H.; Green, M. A.; Ferrazza, F. 19.8% efficient 'honeycomb' textured multicrystalline and 24.4% monocrystalline silicon solar cells. *Appl. Phys. Lett.* **1998**, *73*, 1991–1993.

[18] Hoex, B.; Peeters, F. J. J.; Creatore, M.; Blauw, M. A.; Kessels, W. M. M.; van de Sanden, M. C. M. High-rate plasma-deposited SiO_2 films for surface passivation of crystalline silicon. *J. Vac. Sci. Technol. A* **2006**, *24*, 1823–1830.

[19] Lauinger, T.; Schmidt, J.; Aberle, A. G.; Hezel, R. Record low surface recombination velocities on 1 Ω·cm p-silicon using remote plasma silicon nitride passivation. *Appl. Phys. Lett.* **1996**, 68, 1232–1234.

[20] Aberle, A. G.; Hezel, R. Progress in low-temperature surface passivation of silicon solar cells using remote-plasma silicon nitride. *Prog. Photovolt. Res. Appl.***1997**, *5*, 29–50.

[21] Wolf, S. D.; Agostinelli, G.; Beaucarne, G.; Vitanov, P. Influence of stoichiometry of direct plasma-enhanced chemical vapor deposited SiN_x films and silicon substrate surface roughness on surface passivation. *J. Appl. Phys.* **2005**, *97*, 063303.

[22] Agostinelli, G.; Delabie, A.; Vitanov, P.; Alexieva, Z.; Dekkers, H. F. W.; Wolf, S. D.; Beaucarne, G. Very low surface recombination velocities on p-type silicon wafers passivated with a dielectric with fixed negative charge. *Sol. Energy Mat. Sol. Cells* **2006**, *90*, 3438–3443.

[23] Hoex, B.; Heil, S. B. S.; Langereis, E.; van de Sanden, M. C. M.; Kessels, W. M. M. Ultralow surface recombination of c-Si substrates passivated by plasma-assisted atomic layer deposited Al_2O_3. *Appl. Phys. Lett.* **2006**, *89*, 042112.

[24] Hoex, B.; Gielis, J. J. H.; van de Sanden, M. C. M.; Kessels, W. M. M. On the c-Si surface passivation mechanism by the negative-charge-dielectric Al_2O_3. *J. Appl. Phys.* **2008**, *104*, 113703.

[25] Chen, Z.; Sana, P.; Salami, J.; Rohatgi, A. A novel and effective PECVD SiO_2/SiN antireflection coating for Si solar cells. *IEEE Trans. Electron. Devices* **1993**, *40*, 1161–1165.

[26] Güder, F.; Yang, Y.; Krüger, M.; Stevens, G. B.; Zacharias, M. Atomic layer deposition on phase-shift lithography generated photoresist patterns for 1D nanochannel fabrication. *ACS Appl. Mater. Interfaces* **2010**, *2*, 3473–3478.

[27] Subannajui, K.; Güder, F.; Zacharias, M. Bringing order to the world of nanowire devices by phase shift lithography. *Nano Lett.* **2011**, *11*, 3513–3518.

[28] Wang, F.; Weaver, K. E.; Lakhtakia, A.; Horn, M. W. Electromagnetic modeling of near-field phase-shifting contact lithographywith broadband ultraviolet illumination. *Optik* **2005**, *116*, 1–9.

[29] Sinton, R. A.; Cuevas, A. Contactless determination of current-voltage characteristics and minority carrier lifetimes in semiconductors from quasi-steady-state photoconductance data. *Appl. Phys. Lett.* **1996**, *69*, 2510–2512.

[30] PVEducation. General properties of silicon. http://pveducation.org/pvcdrom/materials/general-properties-of-silicon (accessed Oct 7, 2013).

[31] Lanford, W. A.; Rand, M. J. The hydrogen content of plasma-deposited silicon nitride. *J. Appl. Phys.* **1978**, *49*, 2473–2477.

[32] Mäckel, H.; Lüdemann, R. Detailed study of the composition of hydrogenated SiN_x layers for high-quality silicon surface passivation. *J. Appl. Phys.* **2002**, *92*, 2602–2609.

[33] Reed, M. L.; Plummer, J. D. Chemistry of Si-SiO_2 interface trap annealing. *J. Appl. Phys.* **1988**, *63*, 5776–5793.

[34] Dingemans, G.; Mandoc, M. M.; Bordihn, S.; van de Sanden, M. C. M.; Kessels, W. M. M. Effective passivation of Si surfaces by plasma deposited SiO_x/a-SiN_x:H stacks. *Appl. Phys. Lett.* **2011**, *98*, 222102.

[35] Mawhinney, D. B.; Glass Jr., J. A.; Yates Jr., J. T. FTIR study of the oxidation of porous silicon. *J. Phys. Chem. B* **1997**, *101*, 1202–1206.

[36] Matsunaga, K.; Tanaka, T.; Yamamoto, T.; Ikuhara, Y. First-principles calculations of intrinsic defects in Al_2O_3. *Phys. Rev. B* **2003**, *68*, 085110.

[37] Hang, Q. L.; Wang, F. D.; Buhro, W. E.; Janes, D. B. Ambipolar conduction in transistors using solution grown InAs nanowires with Cd doping. *Appl. Phys. Lett.* **2007**, *90*, 062108.

[38] Weis, K.; Wirths, S.; Winden, A.; Sladek, K.; Hardtdegen, H.; Lüth, H.; Grützmacher, D.; Schäpers, T. Quantum dots in InAs nanowires induced by surface potential fluctuations. *Nanotechnology* **2014**, *25*, 135203.

[39] nextnano^3. http://www.nextnano.com/nextnano3/index.htm (accessed Sep 11, 2013).

[40] Oskooi, A. F.; Roundy, D.; Ibanescu, M.; Bermel, P.; Joannopoulos, J. D.; Johnson, S. G. MEEP: A flexible free-software package for electromagnetic simulations by the FDTD method. *Comput. Phys. Commun.* **2010**, *181*, 687–702.